



1

2 First-order event plane correlated directed and 3 triangular flow from fixed-target energies at 4 RHIC-STAR

4

5 Sharang Rav Sharma (for the STAR Collaboration)

5

Indian Institute of Science Education and Research (IISER) Tirupati

6

January 26, 2024

6

7 Abstract

7

8 We report the measurement of first-order event plane correlated directed flow (v_1)
9 and triangular flow (v_3) for identified hadrons (π^\pm , K^\pm , and p), net-particle (net-K,
10 net-p), and light nuclei (d and t) in Au+Au collisions at $\sqrt{s_{NN}} = 3.2, 3.5, \text{ and } 3.9$ GeV
11 in fixed-target mode from the second phase of beam energy scan (BES-II) program at
12 RHIC-STAR. The v_1 slopes at mid-rapidity for identified hadrons and net-particles
13 except π^+ are found to be positive, implying the effect of dominant repulsive baryonic
14 interactions. The slope of v_1 for net-kaon undergoes a sign change from negative to
15 positive at a lower collision energy compared to net-proton. An approximate atomic
16 mass number scaling is observed in the measured v_1 slopes of light nuclei at mid-
17 rapidity, which favours the nucleon coalescence mechanism for the production of light
18 nuclei. The v_3 slope for all particles decreases in magnitude with increasing collision
19 energy, suggesting a notable integrated impact of the mean-field, baryon stopping, and
20 collision geometry at lower collision energies.

20

21 1 Introduction

22 The primary objective of ultra-relativistic heavy-ion collisions at the Relativistic Heavy
 23 Ion Collider (RHIC) and the Large Hadron Collider (LHC) is to create and characterize a
 24 novel state of matter with partonic degrees of freedom, known as the Quark-Gluon Plasma
 25 (QGP). This state of strongly interacting matter is hypothesized to have been present
 26 during the initial microseconds following the Big Bang, and gaining an understanding of
 27 its properties holds the potential to offer insights into the evolution of the universe [1].
 28 The lattice Quantum Chromodynamics (QCD) predicts a crossover region between the
 29 hadron gas and QGP at higher temperature (T) and low baryon chemical potential (μ_B)
 30 [3]. At lower temperatures and higher μ_B , QCD-based models suggest a first-order phase
 31 transition concluding at a conjectured QCD critical point [4]. Numerous experimental
 32 observables measured at RHIC and LHC have presented compelling evidence of QGP
 33 formation for matter near $\mu_B = 0$. However, experimental confirmation of the existence of
 34 a critical point and a first-order phase transition at higher μ_B is still pending.
 35 Numerous signatures of QGP formation and associated characteristics of the medium have
 36 been proposed. This paper will briefly delve into one of the suggested signatures, namely,
 37 anisotropic flow. The patterns of azimuthal anisotropy in particle production are commonly
 38 referred to as flow. The azimuthal anisotropy in particle production stands out as one of
 39 the most distinct experimental signature of collective flow in heavy-ion collisions. It can
 40 be obtained by studying the Fourier expansion of the azimuthal angle (ϕ) distribution of
 41 produced particles with respect to the event plane angle (Ψ_n).

42 The particle azimuthal angle distribution is written in the form of a Fourier series [4],

$$E \frac{d^3N}{dp^3} = \frac{d^2N}{2\pi p_T dp_T dy} \left\{ 1 + \sum_{n \geq 1} 2v_n \cos[n(\phi - \Psi_n)] \right\}, \quad (1)$$

43 where p_T , y , ϕ , and Ψ_n are particle transverse momentum, rapidity, azimuthal angle of the
 44 particle and the n^{th} order event plane angle, respectively. The various (order n) coefficients
 45 in this expansion are defined as:

$$v_n = \langle \cos[n(\phi - \Psi_n)] \rangle \quad (2)$$

46 The angular brackets in the definition denote an average over many particles and events
 47 [4]. The sine terms in the distribution become zero due to the reflection symmetry con-
 48 cerning the reaction plane.

49 The flow anisotropy parameters (v_n) offer an insight into collective hydrodynamic expan-
 50 sion and transport properties of the produced medium at higher collision energies, while
 51 they are sensitive to the compressibility of the nuclear matter and nuclear EOS at lower

52 collision energies. The first three Fourier expansion coefficients v_1 (directed flow), v_2 (el-
53 liptic flow) and v_3 (triangular flow) are sensitive probes for studying the properties of the
54 matter created in high-energy nuclear collisions.

55 At higher energies (nucleon-nucleon center-of-mass energy $\sqrt{s_{NN}} \gtrsim 27$ GeV), where the
56 transit time of colliding nuclei $2R/\gamma\beta$ (where R is the radius of the nucleus, γ is the Lorentz
57 factor, and β is the velocity of the nuclei) is smaller than the typical production time of
58 particles [5], flow harmonics are predominantly influenced by the collective expansion of
59 the initial partonic density distribution [6]. Conversely, at lower energies, the shadowing
60 effect caused by passing spectator nucleons becomes significant. For $\sqrt{s_{NN}} \lesssim 4$ GeV, nu-
61 clear mean-field effects contribute to the observed azimuthal anisotropies [7]. Numerous
62 studies indicate that flow coefficients are notably sensitive to the incompressibility of nu-
63 clear matter (κ) in the high baryon density region [8]. Comparing experimental data with
64 results from theoretical transport models can provide constraints on κ , offering valuable
65 insights into nuclear EOS.

66 The directed flow (v_1), sensitive to early collision dynamics, is proposed as a signature
67 of first-order phase transition based on a hydrodynamic calculations. These calculations,
68 whose EOS incorporates a first-order phase transition from hadronic matter to QGP,
69 predict a non-monotonic variation of the slope of the directed flow of baryons (and net-
70 baryons) around midrapidity as a function of beam energy [9].

71 The traditional v_3 , third order flow coefficient typically results from fluctuations in shape of
72 the initial condition and is not correlated to the reaction plane. In contrast to this, initial
73 observations were made by HADES, followed by the STAR collaboration, in Au+Au colli-
74 sions at $\sqrt{s_{NN}} = 2.4$ GeV and 3 GeV, respectively. A noticeable triangular flow, correlated
75 with the first order event plane (Ψ_1) was observed [6].

76 The v_3 is also observed to be sensitive to the EOS and can serve as a new tool to explore
77 the time dependence of the pressure during the heavy-ion collision [10]. The evolution of
78 v_3 is influenced by two crucial factors: the first involves the appropriate geometry deter-
79 mined by stopping, the passing time of spectators, and the expansion of the fireball; the
80 second entails a potential within the responsive medium that propels the collective motion
81 of particles.

82 **2 STAR Fixed-Target Program**

83 The fixed target (FXT) setup was implemented at Solenoidal Tracker at RHIC (STAR)
84 to explore the region of high μ_B on the QCD phase diagram. This data was collected
85 during the second phase of the Beam Energy Scan program (BES-II) (2019-2020) after
86 incorporating various detector upgrades.

87 2.1 Experimental Setup

88 The STAR FXT comprises a 0.25 mm thick gold foil (equivalent to a 1% nuclear interaction
89 probability) mounted on a half collar with two aluminum support rods. Positioned at
90 the west edge of the TPC, the target is longitudinally 200 cm away from the nominal
91 interaction point at the center of the TPC. Placed at the bottom of the beam pipe,
92 the top edge of the gold foil is situated 2 cm below the center of the beam pipe. This
93 configuration is crucial to prevent unintended collisions between the beam and the target
94 during collider mode operation. In fixed-target mode, the accelerator technicians lowered
95 the beam by 1.8 cm until the trigger rate reached 2 kHz, which is the limit of the Data
96 Acquisition (DAQ) system.

97 During fixed-target mode operation, the accelerator utilizes only one cycling beam. In
98 this setup, the beam is filled with only 12 bunches, with each bunch containing 7×10^9
99 ions. This limitation on the number of bunches serves to separate out-of-time pileup by a
100 sufficiently large distance and also restricts the DAQ rate. The rationale behind limiting
101 the number of bunches is to avoid instances where two collisions occur too close together
102 temporally. In such cases, the vertices may appear too close together longitudinally in the
103 TPC and might be reconstructed as a single vertex with a multiplicity equal to the sum of
104 the two independent collision multiplicities. To prevent these out-of-time pileup vertices,
105 a reduction in the number of bunches ensures spatial separation.

106 2.2 Fixed-Target Conventions

107 In contrast to collider mode collisions, in FXT collisions in the STAR coordinate system,
108 the target is situated at the edge of TPC, and midrapidity is not zero. To convert the
109 measured rapidity (y) in the coordinate system to the rapidity in the center of mass frame
110 (y_{cms}), it is necessary to boost the measured rapidity by the beam rapidity. The beam
111 rapidity (y_b) for a given center of mass energy is calculated by the equation,

$$y_b = \cosh^{-1} \left[\frac{\sqrt{s_{NN}}}{2m_p} \right], \quad (3)$$

112 where the $\sqrt{s_{NN}}$ is center of mass energy (e.g. 3.2 GeV), and the m_p is proton mass (0.938
113 GeV). In STAR convention, the beam-going direction is the positive direction (the target
114 is located in the negative rapidity direction for 3.2 GeV at $y_b = -1.127$). To match the
115 STAR conventions, when calculating rapidity in the center of the mass frame and shifting
116 by midrapidity, we also need to flip the sign of rapidity.

$$y_{cms} = -(y_{lab} - y_b). \quad (4)$$

118 3 Dataset and Event Selection Cuts

119 In this paper, we present the results of first order event plane (Ψ_1) correlated v_1 and
120 v_3 for identified hadrons (π^\pm , K^\pm , and p), net-particle (net-K, net-p), and light nuclei (d
121 and t) in Au+Au collisions at $\sqrt{s_{NN}} = 3.2, 3.5,$ and 3.9 GeV using the FXT data from
122 the STAR experiment. In FXT mode, we apply a vertex cut along the z-direction (v_z)
123 within [198, 202] cm. For the x and y directions, we set the V_r ($\sqrt{V_x^2 + V_y^2}$) less than 2
124 cm centered around (0, -2).

125 4 Analysis Details

126 4.1 Track Quality Cuts

127 To ensure the quality of primary tracks, tracks with the transverse momentum $p_T < 0.2$
128 GeV/c are excluded. Additionally, we mandate the utilization of a minimum of 15 fit
129 points and 52% of the total possible fit points in the track fitting process. The selection
130 criterion involves choosing dE/dx hit points ≥ 10 . Furthermore, the distance of closest
131 approach (DCA) is set to < 3 cm.

132 4.2 Particle Identification

133 The identification of charged particles in STAR is done by the combination of Time Projec-
134 tion Chamber (TPC) and Time of Flight (TOF) detectors. For low-momentum particles,
135 TPC is used, whereas for particles with intermediate or high momenta ($p_T > 1$ GeV/c),
136 the TOF is used. TPC uses the ionization energy loss (dE/dx) of the charged particles
137 passing through it for particle identification. Using dE/dx information, the z variable is
138 defined:

$$z = \ln\left(\frac{\langle dE/dx \rangle}{\langle dE/dx \rangle_X^B}\right), \quad (5)$$

139 where $\langle dE/dX \rangle_X^B$ is the expected energy loss based on the Bichsel function and X is the
140 particle type [11]. The raw yield from the TOF are obtained using the variable mass square
141 (m^2), given by

$$m^2 = p^2 \left(\frac{c^2 T^2}{L^2} - 1 \right), \quad (6)$$

142 where, p, T, L, and c are the momentum, time of travel by the particle, path length and
143 speed of light, respectively. The left panel of Fig 1 shows the average dE/dx of measured
144 charged particles plotted as a function of “rigidity” (i.e., momentum/charge) of the parti-
145 cles. The curves represent the Bichsel expectation values. The right panel of Fig 1 shows
146 the inverse of particle velocity in unit of the speed of light $1/\beta$, as a function of rigidity.
147 The expected values of $1/\beta$ for charged particles are shown as the curves.

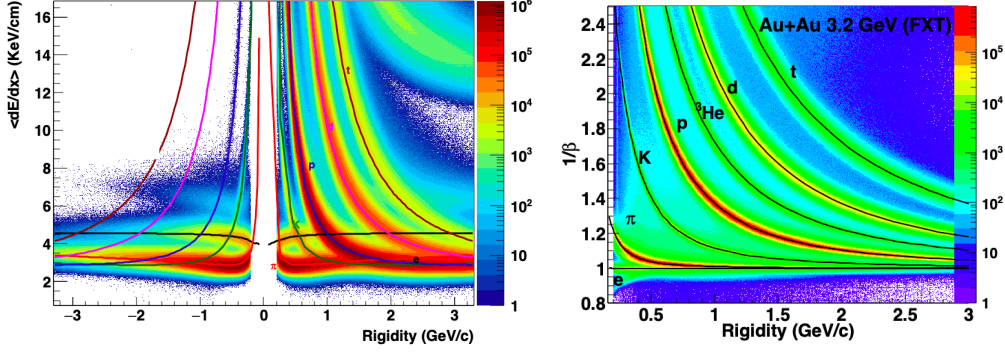


Figure 1: $\langle dE/dx \rangle$ from TPC (left panel) and $1/\beta$ from TOF (right panel) for charged particles in Au+Au collisions at $\sqrt{s_{NN}} = 3.2$ GeV.

148 In this analysis, for the identification of pion, kaon, and proton, we require TPC $n\sigma$
 149 (z/R ; R: TPC resolution) and TOF m^2 cuts which are listed in the Table 1. In addition to
 150 m^2 cut a momentum dependent z cut is implemented for light nuclei identification.

Table 1: Particle identification cuts

pion	$ n\sigma_\pi < 3$ and $-0.1 < m^2 < 0.15$ ($(GeV/c^2)^2$)
kaon	$ n\sigma_K < 3$ and $0.16 < m^2 < 0.36$ ($(GeV/c^2)^2$)
151 proton	$ n\sigma_p < 2$ and $-0.6 < m^2 < 1.2$ ($(GeV/c^2)^2$)
deuteron	momentum dependent z cut and $3.15 < m^2 < 3.88$ ($(GeV/c^2)^2$)
triton	momentum dependent z cut and $7.01 < m^2 < 8.75$ ($(GeV/c^2)^2$)

152 4.3 Event Plane Reconstruction

153 The event plane angle can be estimated from the particle azimuthal distribution on an
 154 event-by-event basis. In our calculations, we have used the first-order event plane angle
 155 Ψ_1 , which is measured using the Event Plane Detector (EPD). EPD is designed to measure
 156 the pattern of forward-going charged particles emitted in a high-energy collision between
 157 heavy nuclei. In order to calculate the first-order event plane angle, firstly, we construct
 158 the Q vector from particle's azimuthal angle.

$$\vec{Q} = (Q_x, Q_y) = \left(\sum_i w_i \cos(\phi_i), \sum_i w_i \sin(\phi_i) \right), \quad (7)$$

159 The first-order event plane angle ψ_1 is defined as:

$$\psi_1 = \tan^{-1}(Q_y/Q_x), \quad (8)$$

160 where sum extends over all detected hits i , and ϕ_i is the azimuthal angle in the laboratory
 161 frame, and w_i is the weight for the i^{th} hits, here we use the nMip as the weight, which is

162 the calibrated ADC value. In order to mitigate acceptance correlations arising from the
 163 imperfect detector, it is essential to render the event plane angle distribution isotropic or
 164 flat. Consequently, a procedure for flattening the event plane angle distribution becomes
 165 necessary. In this analysis, we have implemented re-centering and shift corrections to ex-
 166 tract a flat event plane angle distribution [4].

167 In the re-centering correction, the Q-vector averaged over multiple events is subtracted
 168 from the Q-vector of each individual event. Subsequently, the event plane angle is cal-
 169 culated. However, performing only the re-centering correction is insufficient. After the
 170 implementation of re-centering, a shift correction is additionally applied to ensure that
 171 the event plane angle distribution becomes flat. In shift correction, one fits the non-flat
 172 distribution of ψ_n averaged over many events with a Fourier expansion and calculates the
 173 shifts for each event ψ_n necessary to force a flat distribution on average. The re-centering
 174 and shift correction are all performed run-by-run and centrality-by-centrality in this anal-
 175 ysis.

176 4.4 Event Plane Resolution

177 The finite number of detected particles in detectors produces a limited resolution in
 178 the measured event plane angle. So, the observed flow coefficients must be corrected up
 179 to what they would be relative to the real reaction plane. This is done by dividing these
 180 coefficients by the event plane resolution, estimated from the correlation of the planes of
 181 independent subevents.

$$v_n = \frac{v_n^{obs}}{R_n} = \frac{v_n^{obs}}{\langle \cos[n(\psi_n - \Psi_R)] \rangle}, \quad (9)$$

182 where the R_n is resolution, v_n is the n^{th} harmonic azimuthal anisotropy parameter, and
 183 ψ_n is the n^{th} harmonic order event plane, Ψ_r is reaction plane angle. The angle brackets
 184 denote an average over all particles in all events [4].

185 In fixed target mode, the final state particle's acceptance is not symmetric around midra-
 186 pidity. Therefore, the commonly used 2-sub event method, employed in the collider BES-I
 187 analysis, cannot be used to calculate the resolution. This method necessitates each sub-
 188 event to have similar multiplicity and resolution. Consequently, in this analysis, we opt
 189 for the 3-sub event method to calculate the resolution. Figure 2 shows the calculated first-
 190 order event plane resolution R_{11} and the third-order event plane resolution R_{13} estimated
 191 from the first-order event plane for v_3 calculation, as functions of collision centrality.

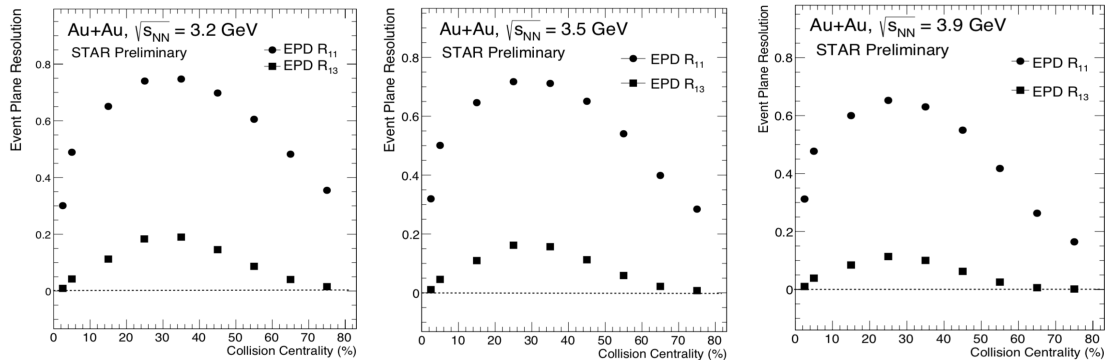


Figure 2: Collision centrality dependence of R_{11} (circles) R_{13} (squares) in Au+Au collisions at $\sqrt{s_{NN}} = 3.2$ (left panel), 3.5 (middle panel), and 3.9 GeV (right panel).

192 5 Systematic Uncertainties

193 The systematic uncertainties associated with the measured flow harmonics stem from
 194 the charged track selection method, particle identification, and event plane resolution.
 195 These uncertainties are evaluated point-by-point on v_1 and v_3 as a function of y for each
 196 identified hadron and light nuclei. The systematic uncertainties arising from track selection
 197 are assessed by varying the selection requirements. Those linked to particle misidentifi-
 198 cation are determined by varying the z and m^2 cuts. A common systematic uncertainty
 199 arising from event plane resolution is assessed by employing combinations of different η
 200 sub-events. In the subsequent figures, the shaded boxes represent the total systematic
 201 uncertainty for each data point.

202 6 Results and Discussion

203 6.1 Directed Flow (v_1)

204 The rapidity (y), centrality and collision energy dependence of v_1 for identified hadrons,
 205 net-particle, and light nuclei are measured at $\sqrt{s_{NN}} = 3.2, 3.5,$ and 3.9 GeV.
 206 Figure 3 illustrates the the centrality dependence of π^+ for $\sqrt{s_{NN}} = 3.2$ GeV. The v_1
 207 changes sign from negative to positive, moving from most central to peripheral collisions,
 208 implying the effect of dominant repulsive baryonic interactions and spectator shadowing.
 209 The energy dependence of proton v_1 involves an interplay between the directed flow of
 210 protons associated with baryon stopping and particle-antiparticle pair production at mid-
 211 rapidity. A means to distinguish between the two mechanisms would thus be to look at
 212 the net particle v_1 . The net particle represents the excess yield of a particle species over

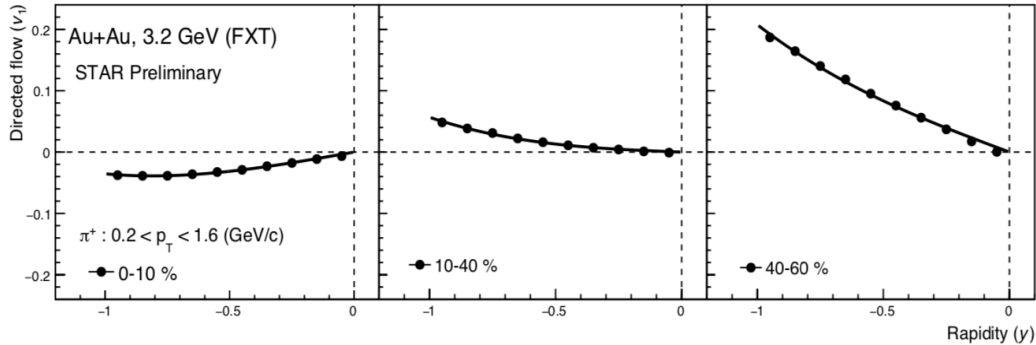


Figure 3: v_1 as a function of y for pion in 0-10% (left panel), 10-40 % (middle panel), and 40-60% (right panel) centrality bin in Au+Au collisions at $\sqrt{s_{NN}} = 3.2$ GeV. The line represents third order polynomial fit to distribution.

213 its antiparticle. The net particle's v_1 is defined as

$$v_{1,net} = \frac{v_{1,p} - r v_{1,\bar{p}}}{1 - r}, \quad (10)$$

214 where $v_{1,p}$, $v_{1,\bar{p}}$ corresponds to v_1 of particle and anti-particle, and r represents the ratio
215 of anti-particles to particles [9].

216 In relativistic heavy-ion collisions, the production of light nuclei can occur through two
217 mechanisms. The first mechanism involves the direct production of nucleus-antinucleus
218 pairs in elementary nucleon-nucleon (NN) or parton-parton interactions. Due to their
219 small binding energies, the directly produced nuclei or antinuclei are likely to undergo
220 dissociation in the medium before escaping. The second and presumably dominant mech-
221 anism for the production of nuclei and antinuclei is through the final state coalescence of
222 produced nucleons and antinucleons or participant nucleons [13]. In this process, nucleons
223 and antinucleons combine to form light nuclear and antinuclear clusters during the final
224 stages of kinetic freeze-out. The probability of formation is proportional to the product
225 of the phase space densities of its constituent nucleons [14]. Therefore, the production of
226 light nuclei yields information about the size of the emitting system and its space-time
227 evolution. Due to the longer passing time of the colliding ions in the few GeV regime, the
228 interference between the expanding central fireball and the spectator remnants becomes
229 more significant than at higher energies.

230 Figure 4 shows the y dependence of identified hadrons (left panel), net-particles (middle
231 panel), and light nuclei (right panel) for 10–40% centrality. The magnitude of v_1 increases
232 with increasing rapidity for all particles, and a mass ordering is also observed in the mag-
233 nitude of v_1 .

234 The p_T -integrated $v_1(y)$ slope at mid-rapidity, $dv_1/dy|_{y=0}$, is obtained by fitting the data
235 $v_1(y)$ with a third-order polynomial. Figure 5 shows the collision energy dependence of

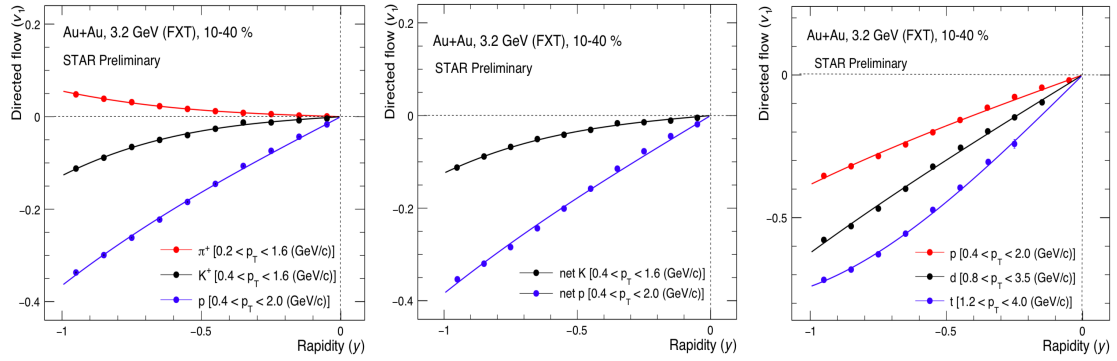


Figure 4: v_1 as a function of y in 10–40% centrality for identified hadrons (left panel), net particles (middle panel) and light nuclei (right panel) in Au+Au collisions at $\sqrt{s_{\text{NN}}} = 3.2$ GeV. The line represents 3rd order polynomial fit to distribution.

236 $dv_1/dy|_{y=0}$ for identified particles (left panel), net-particle (middle panel), and light nu-
 237 clei (right panel) in mid-central (10 - 40%) collisions. The extracted slope parameters,
 238 $dv_1/dy|_{y=0}$, are scaled by A for light nuclei to compare with protons. The magnitude of
 239 the slope decreases with increasing collision energy for all particles, including net-particles
 240 and light nuclei.

241 At low energies, the transit time (τ) is comparable to the formation time of particles.
 242 Consequently, the spectators are not sufficiently distant from the collision volume, and the
 243 medium does not have the freedom to expand freely. This results in interactions between
 244 baryon-dominated spectator particles and the produced particles. Among the produced
 245 particles, pions, being one of the lightest, are particularly affected. The flow for π^+ is ob-
 246 structed by the spectator particles, leading to a negative value for its v_1 slope. In contrast,
 247 π^- , influenced by Coulomb interactions from the baryons (protons), acquires a positive v_1
 248 slope value.

249 The slope of v_1 for net-kaon undergoes a sign change from negative to positive at a lower
 250 collision energy range ($\sqrt{s_{\text{NN}}} = 3.9 - 7.7$ GeV) compared to net-proton ($\sqrt{s_{\text{NN}}} = 11.5 -$
 251 19.6 GeV).

252 The light nuclei v_1 slope exhibits an approximate mass number (A) scaling, consistent
 253 with the nucleon coalescence mechanism for the production of light nuclei at low collision
 254 energies.

255 6.2 Triangular Flow (v_3)

256 The y and collision energy dependence of v_3 for identified hadrons and light nuclei are
 257 measured at $\sqrt{s_{\text{NN}}} = 3.2, 3.5, \text{ and } 3.9$ GeV. The left panel of Fig. 6 shows the rapidity
 258 dependence of v_3 for identified hadrons. The magnitude of v_3 increases with increasing

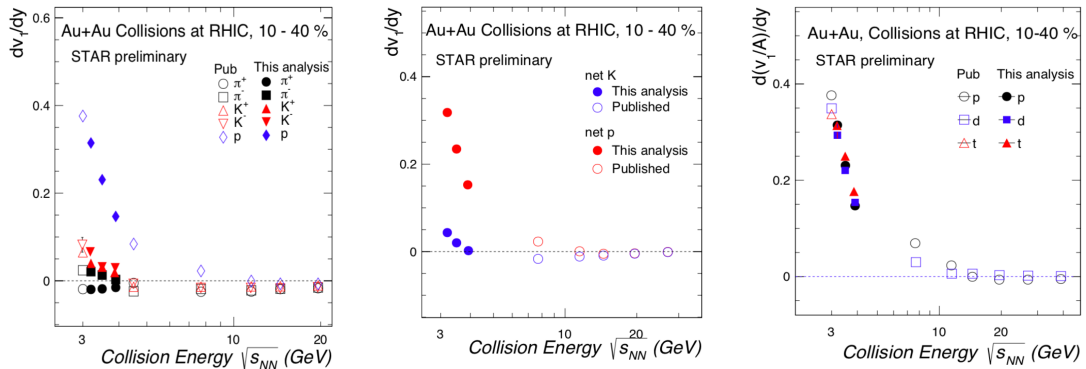


Figure 5: Collision energy dependence of v_1 slope $dv_1/dy|_{y=0}$ for identified hadrons (left panel), net particles (middle panel) and light nuclei (right panel) in Au+Au collisions at RHIC for 10 – 40% centrality. The published data are shown in open markers [12].

259 rapidity. The distribution is fitted with a polynomial of order three to extract the slope
 260 parameter.

261 The middle panel of Fig. 6 shows the slope of v_3 , $dv_3/dy|_{y=0}$, for identified hadrons as a
 262 function of collision energy. The magnitude of $dv_3/dy|_{y=0}$ decreases with increasing colli-
 263 sion energy. It may indicates that the combined effect of the mean-field, baryon stopping,
 264 and collision geometry is considerably significant at the low collision energies [15].

265 The right panel of Fig. 6 shows the extracted slope parameters, $dv_3/dy|_{y=0}$, scaled by mass
 266 number (A) for light nuclei. The magnitude of the slope decreases with increasing collision
 267 energy. The light nuclei v_3 slope also exhibits an approximate mass number (A) scaling
 268 within systematic uncertainties, consistent with the nucleon coalescence mechanism for
 269 the light nuclei production.

270 7 Conclusion

271 In summary, the rapidity, centrality, and collision energy dependence of directed flow
 272 (v_1) of identified hadrons, net particle, and light nuclei in Au+Au collisions at $\sqrt{s_{NN}} = 3.2$,
 273 3.5, and 3.9 GeV is reported. The magnitude of v_1 increases with increasing rapidity for all
 274 particles. The extracted v_1 slope of all the particles decreases in magnitude with increasing
 275 collision energy. A positive v_1 slope at mid-rapidity for identified hadrons and net particles,
 276 excluding π^+ , suggests prevalent repulsive baryonic interactions and spectator shadowing.
 277 As collision energy decreases, a non-monotonic trend is observed in the slope of both net-
 278 kaon and net-proton. The v_1 slope for net-kaon experiences a transition from negative to
 279 positive at a collision energy lower than that observed for net-proton. The light nuclei v_1
 280 slope exhibits an approximate mass number scaling consistent with the nucleon coalescence

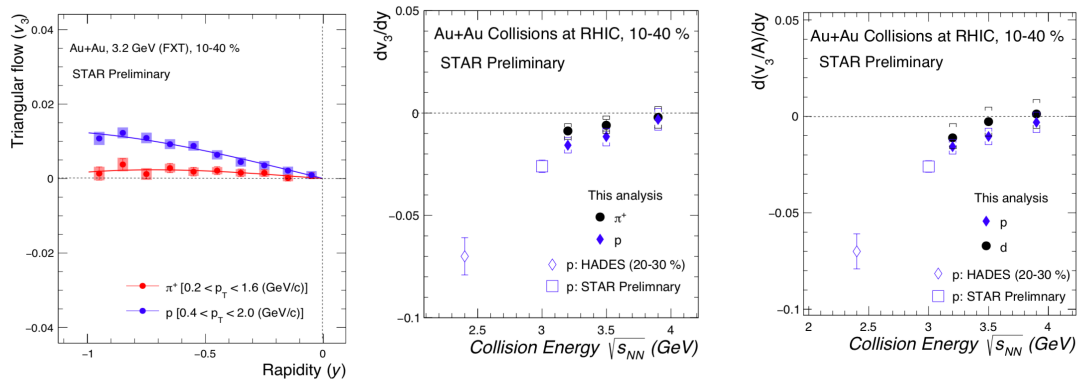


Figure 6: v_3 as a function of y in 10–40% centrality bin for identified hadrons (left panel) in Au+Au collisions at $\sqrt{s_{NN}} = 3.2$ GeV. Collision energy of $dv_3/dy|_{y=0}$ for identified particles (middle panel) and light nuclei (right panel) in Au+Au collisions at RHIC for 10 – 40% centrality. The published data are shown in open markers [10].

281 mechanism for the production of light nuclei. The magnitude of slope of v_3 decreases
 282 with increasing collision energy, indicating a substantial collective impact of the mean-
 283 field, baryon stopping, and collision geometry at lower collision energies. Similar to the v_1
 284 slope of light nuclei, the v_3 slope of light nuclei also displays an approximate scaling with
 285 mass number (A) within the systematic uncertainties. This trend supports the nucleon
 286 coalescence mechanism as a favorable explanation for the production of light nuclei.

287 References

- 288 [1] H. Kastrup, P. Zerwas, eds., QCD - 20 yrs later, World Scientific, Singapore (1993).
- 289 [2] A. Aprehian et. al. DOE/NSF Nuclear Science Advisory Panel (NSAC) Report,
 290 (2015).
- 291 [3] F.R. Brown, et. al., Phys. Rev. Lett. 65, 2491 (1990).
- 292 [4] A. M. Poskanzer and S. A. Voloshin, Phys. Rev. C 58, 1671 (1998).
- 293 [5] A. Bialas, M. Gyulassy, Nucl. Phys. B 291, 793 (1987).
- 294 [6] B. I. Abelev et al. (STAR Collaboration), Phys. Rev. Lett. 99, 112301 (2007).
- 295 [7] H. Liu et al. (E895 Collaboration), Phys. Rev. Lett. 84, 5488 (2000).
- 296 [8] P. Danielewicz, R. Lacey, and W. G. Lynch, Science 298, 1592 (2002).
- 297 [9] H. Sorge, Phys. Rev. Lett. 78, 2309 (1997).

- 298 [10] J. Adamczewski-Musch et al. (HADES), Phys. Rev. Lett. 125, 262301 (2020).
- 299 [11] H. Bichsel, Nucl. Instrum. Meth. A 562, 154 (2006).
- 300 [12] L. Adamczyk et al. (STAR Collaboration), Phys. Rev. Lett. 120, 062301 (2018).
- 301 [13] H.H. Gutbrod et al., Phys. Rev. Lett. 37, 667 (1976).
- 302 [14] L. P. Csernai and J. I. Kapusta, Phys. Rep. 131, 223 (1986); A. Z. Mekjian, Phys.
303 Rev. C 17, 1051 (1978).
- 304 [15] STAR Collaboration arXiv: 2309.12610 [nucl-ex] (2023).